J. Fluid Mech. (1988), *vol.* 190, *pp.* 87–112
Printed in Great Britain

Flow in a channel with a moving indentation

By M. E. RALPH† AND T. J. PEDLEY
Department of Applied Mathematics and Theoretical Physics, University of Cambridge,
Silver Street, Cambridge CB3 9EW, UK

(Received 23 February 1987 and in revised form 30 November 1987)

The unsteady flow of a viscous, incompressible fluid in a channel with a moving indentation in one wall has been studied by numerical solution of the Navier–Stokes equations. The solution was obtained in stream-function–vorticity form using finite differences. Leapfrog time-differencing and the Dufort–Frankel substitution were used in the vorticity transport equation, and the Poisson equation for the stream function was solved by multigrid methods. In order to resolve the boundary-condition difficulties arising from the presence of the moving wall, a time-dependent transformation was applied, complicating the equations but ensuring that the computational domain remained a fixed rectangle.

Downstream of the moving indentation, the flow in the centre of the channel becomes wavy, and eddies are formed between the wave crests/troughs and the walls. Subsequently, certain of these eddies 'double', that is a second vortex centre appears upstream of the first. These observations are qualitatively similar to previous experimental findings (Stephanoff *et al.* 1983, and Pedley & Stephanoff 1985), and quantitative comparisons are also shown to be favourable. Plots of vorticity contours confirm that the wave generation process is essentially inviscid and reveal the vorticity dynamics of eddy doubling, in which viscous diffusion and advection are important at different stages. The maximum magnitude of wall vorticity is found to be much larger than in quasi-steady flow, with possibly important biomedical implications.

1. Introduction

Detailed knowledge of unsteady separated flow in tubes with localized time-dependent constrictions is thought to be an important prerequisite for understanding the self-excited oscillations that develop when fluid flows through an externally compressed collapsible tube (see Cancelli & Pedley 1985, and references therein). Also the time- and space-dependent shear stress exerted by flowing blood on the walls of non-uniform arteries is important in the early stages of atherosclerosis (Ku *et al.* 1985), and needs to be better understood. In an approach to these problems, experiments have been carried out on flow through a two-dimensional channel in which part of one wall executes *prescribed* in-and-out motions, so that the fluid flow problem is uncoupled from the (complex) solid mechanics of the wall. Visualizations of the flow were first reported by Stephanoff *et al.* (1983) and quantitative measurements were made by Pedley & Stephanoff (1985), hereinafter referred to as SPLS and PS respectively. The main findings were as follows: a train of propagating waves is observed to grow downstream of the moving indentation during each cycle, for a wide range of Strouhal numbers ($St > 0.005$) and Reynolds numbers (Re between 360

---

† Present address: Smith Associates Ltd, Surrey Research Park, Guildford, Surrey, GU2 5YP, UK.

and 1260), and regions of closed streamlines ('eddies') are formed between the sinuous core flow and the walls. Subsequently certain of the eddies (those nearest the moving indentation) 'double', that is a second eddy appears upstream of the first, the timescale for the formation of the second eddy being very short. An inviscid, small-amplitude theory was proposed, and gave good agreement with experimental measurements of wave crest positions, but did not describe eddy doubling. According to the theory, the waves are generated as inviscid perturbations to the vorticity distribution in the oncoming flow, and were therefore referred to as 'vorticity waves'. They can also be thought of as the large-amplitude limit of Tollmien–Schlichting (TS) waves, as analysed by Smith & Burggraf (1985) and discussed by PS. Other theoretical studies of large-amplitude TS waves, in external boundary-layer flow, include those by Duck (1985) and Smith (1986).

Experimental observations of waves in incompressible internal flow include those of Cherdron, Durst & Whitelaw (1978), who found that steady flow through a symmetric expansion in a two-dimensional channel forms large-amplitude asymmetric waves, with eddies underneath, at values of *Re* between 500 and 800. Sobey (1985) repeated some of their observations, and in addition found much stronger asymmetric waves when the flow was oscillatory ($0.004 < St < 0.008$). The eddies in his experiments look very similar to those of PS, and also tend to double. Armaly *et al.* (1983) observed one or two relatively weak standing eddies in steady flow downstream of an asymmetric expansion (a step in one channel wall), but only for a limited range of *Re* ($50 < Re < 640$); flow visualization by Bertram & Pedley (1983) of flow past an asymmetric indentation with sloping ends failed to reveal such eddies in steady flow.

In the present study, the Navier–Stokes equations for an incompressible fluid have been solved numerically for boundary conditions chosen to simulate those of the experiments of SPLS and PS. The motivation is both to verify the numerical technique by an accurate simulation of measured quantities (also providing a check on the somewhat tentative measurements of PS) and to use it to compute quantitative details of the velocity and vorticity fields. Particular attention is paid to eddy doubling, because of its wider applicability, and to predictions of wall vorticity, both for the light it sheds on eddy doubling and because of the importance of wall shear stress in atherogenesis.

The aspect ratio of the channel used in the experiments of SPLS and PS was 10, and features of the flow were observed to be nearly uniform in the spanwise direction over most of the flow cycle, so that a two-dimensional simulation is appropriate. Whilst many solutions of the unsteady Navier–Stokes equations have been described, there are few with moving boundaries. Those who have studied such problems include Viecelli (1971), who adapted the MAC method to solve free-surface and 'flexible-bag' problems; Peskin (1972, 1977) who, in modelling cardiac flows, replaced moving solid boundaries by distributions of force in such a way that the appropriate boundary conditions were satisfied; and Daly (1974) who used a mixed Eulerian–Lagrangian method and studied the propagation of pressure pulses in flexible tubes. In these works, interaction of the fluid and solid mechanics was allowed for, whereas in other contexts, including the present one, the motion of the boundary has been prescribed. Hung & Schuessler (1977), for example, computed inviscid flows in models of prosthetic heart valves. More recently, Robertson, Clark & Cheng (1982) have solved the Navier–Stokes equations for planar channel flow with symmetrical moving boundaries, at Reynolds numbers somewhat smaller than those considered below. Their method was to transform a computational region with a moving boundary of relatively complex shape into a fixed rectangle, thus giving a system of equations with coefficients dependent on both position and time, but with simple boundary conditions. A similar method was developed for the present problem on the basis of techniques used previously for fixed-wall computations (Sobey 1980 and Ralph 1986, for example). Robertson *et al.* did not predict the occurrence of waves, no doubt because symmetry was imposed on the flow, and the largest Reynolds number they considered was about 240 in the present notation, about half of the smallest value considered here.

In the present paper, a full formulation of the problem is given in §2, and the methods of solution described in §3, including an assessment of the effects of the mesh size on computational accuracy. Results for three cases are described in detail and discussed in §4, whilst §5 contains further discussion.

2. Formulation of the problem

The volumetric flow rate $\hat{Q}_0$ per unit channel depth upstream of the moving indentation is taken to be fixed, as in the experiments of SPLS and PS. The unperturbed channel width is $\hat{a}$ and a reference velocity is then

$$\hat{U}_0 = \hat{Q}_0/\hat{a}. \tag{1}$$

The timescale for the oscillations of the moving indentation is the period $1/\hat{f}$, so that the dimensional time is $t/\hat{f}$; $\hat{\nu}$ is the fluid kinematic viscosity. Thus for a given shape and amplitude of wall indentation, the problem is specified by any two among the Reynolds number *Re*, Strouhal number *St*, and frequency parameter α^2, defined by

$$Re = \frac{\hat{U}_0 \hat{a}}{\hat{\nu}}, \quad St = \frac{\hat{a}\hat{f}}{\hat{U}_0}, \quad \alpha^2 = Re\, St. \tag{2}$$

If the longitudinal and transverse coordinates are $\hat{a}(x,y)$, and the corresponding velocity components are $\hat{U}_0\ (\partial\psi/\partial y, -\partial\psi/\partial x)$, where ψ is the stream function, then the governing equation for the vorticity ζ, is

$$\frac{\partial\zeta}{\partial t} = -\frac{1}{St}\left[\frac{\partial\psi}{\partial y}\frac{\partial\zeta}{\partial x} - \frac{\partial\psi}{\partial x}\frac{\partial\zeta}{\partial y}\right] + \frac{1}{\alpha^2}\left[\frac{\partial^2\zeta}{\partial x^2} + \frac{\partial^2\zeta}{\partial y^2}\right], \tag{3}$$

where ζ is defined by

$$-\zeta = \frac{\partial^2\psi}{\partial x^2} + \frac{\partial^2\psi}{\partial y^2}. \tag{4}$$

The walls of the channel are defined to be at $y = 1$ and $y = F(x,t)$, and, as in SPLS and PS, $F(x,t)$ is taken to be of the separable form

$$F(x,t) \equiv g(x)\, h(t), \tag{5}$$

where $h(t) = 0$ for $t < 0$, $h(t) \geqslant 0$ for $t \geqslant 0$, and $g(x) \geqslant 0$. Thus the moving wall is initially flush with the plane $y = 0$, and is never thereafter withdrawn beyond $y = 0$; this constraint is not necessary for the numerical method to work, but is imposed for consistency with the experiments.

In order to simplify application of the boundary conditions, we make the transformation

$$z = \frac{y - F(x,t)}{1 - F(x,t)} \tag{6}$$

so that the boundaries at $y = F$, $y = 1$ become $z = 0$, $z = 1$ respectively. Under this transformation, (3) and (4) become

$$\frac{\partial \zeta}{\partial t} = -\frac{1}{St} p_1 \left[\frac{\partial \psi}{\partial z}\frac{\partial \zeta}{\partial x} - \frac{\partial \psi}{\partial x}\frac{\partial \zeta}{\partial z}\right] + \frac{1}{\alpha^2}\nabla^2 \zeta + p_4 \frac{\partial \zeta}{\partial z} \tag{7}$$

and

$$-\zeta = \nabla^2 \psi, \tag{8}$$

where

$$\nabla^2 \equiv \frac{\partial^2}{\partial x^2} + (p_1^2 + p_2^2)\frac{\partial^2}{\partial z^2} + 2p_2 \frac{\partial^2}{\partial x \partial z} + p_3 \frac{\partial}{\partial z}, \tag{9}$$

$$p_1(x,t) \equiv \frac{1}{1-F}, \tag{10}$$

$$p_2(x,z,t) \equiv -\frac{1-z}{1-F}\frac{\partial F}{\partial x}, \tag{11}$$

$$p_3(x,z,t) \equiv -\frac{1-z}{1-F}\left[\frac{\partial^2 F}{\partial x^2} + \frac{2}{1-F}\left(\frac{\partial F}{\partial x}\right)^2\right] \tag{12}$$

and

$$p_4(x,z,t) \equiv \frac{1-z}{1-F}\frac{\partial F}{\partial t}. \tag{13}$$

The initial condition is imposed when $F = 0$ and is that of Poiseuille flow throughout the channel; that is

$$\zeta = 6(2z-1), \tag{14}$$

$$\psi = z^2(3-2z). \tag{15}$$

At $t = 0$, a portion of the wall $z = 0$ begins to move, with $h(t)$ given by

$$h(t) = \tfrac{1}{2}(1-\cos 2\pi t). \tag{16}$$

The shape of the indentation is described by $g(x)$, where

$$\begin{aligned} g(x) &= 0 && \text{for } x_1 < x < x_2, \\ &= \tfrac{1}{2}\epsilon\{1+\tanh\beta(x-x_a)\} && \text{for } x_2 < x < x_3, \\ &= \epsilon && \text{for } x_3 < x < x_4, \\ &= \tfrac{1}{2}\epsilon\{1-\tanh\beta x\} && \text{for } x_4 < x < x_5, \\ &= 0 && \text{for } x_5 < x < x_6, \end{aligned} \tag{17}$$

and this reproduces approximately the geometry of SPLS and PS if the amplitude parameter ϵ, the slope parameter β, and the parameters $x_i (i = 2, \ldots, 5)$ and x_a are given appropriate values (see figure 1). The origin of the axial coordinate is at the centre of the downstream slope of the indentation. We have taken $\epsilon = 0.38$, $\beta = 4.14$, $(x_3 - x_2) = (x_5 - x_4) = 2.5$, $(x_4 - x_3) = 8$, $x_2 + x_3 = 2x_a$ and $x_4 + x_5 = 0$; that is the size and shape of the indentation have been fixed, but x_1 and x_6 have been varied in order to assess the effects of applying the up- and downstream boundary conditions at finite distances. Note that for $x_1 < x < x_2$ and $x_5 < x < x_6$, $p_1 = 1$ and $p_2 = p_3 = p_4 = 0$, so that (7) and (8) reduce to the form of (3) and (4).

As $F(x,t)$ is separable, the boundary conditions at $y = F(x,t)$ can be written

$$\frac{\partial \psi}{\partial y} = 0 \tag{18}$$

and

$$\frac{\partial \psi}{\partial x} = -St\frac{\partial F}{\partial t}, \tag{19}$$

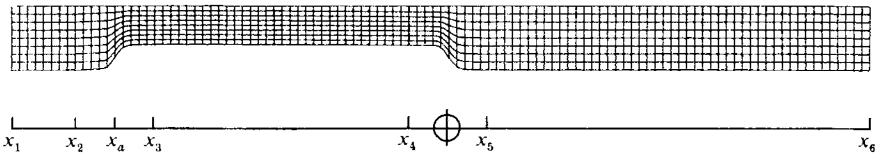

FIGURE 1. Representation of the computational domain. Lines of constant x and constant z are shown at the time of maximum indentation, and the y-scale is expanded by a factor of 2 compared to the x-scale.

so that the condition on ψ at the indented wall is

$$\psi = -St \int_{x_1}^{x} g(x')\,\mathrm{d}x' \frac{\mathrm{d}h}{\mathrm{d}t}. \tag{20}$$

ψ takes the value unity on the boundary at $y = z = 1$.

Conditions on the vorticity at the walls are obtained by substituting into (8) values of the stream-function derivatives such that the fluid velocity components match those of the wall locally. Thus, at $z = 1$, where the wall is at rest, we obtain

$$\zeta|_{z=1} = -p_1^2 \frac{\partial^2 \psi}{\partial z^2}\Big|_{z=1}, \tag{21}$$

whilst at $z = 0$ we have

$$\zeta|_{z=0} = -(p_1^2 + p_2^2) \frac{\partial^2 \psi}{\partial z^2}\Big|_{z=0} + \frac{\partial^2 \psi}{\partial x^2}\Big|_{z=0}. \tag{22}$$

The second term of (22) implies that even in the absence of a mean flow, vorticity is generated by a pulsating hump on which the no-slip condition is satisfied, through the rotations of wall elements.

The upstream and downstream boundary conditions require parallel flow at infinite distance from the indentation, with the upstream flow being of Poiseuille form. How this requirement is translated into conditions at the finite up- and downstream boundaries, x_1 and x_6, of the computation zone is described in the next section.

3. Numerical solution methods

3.1. *Overall solution strategy and the vorticity transport equation*

A standard vorticity–stream-function formulation has been utilized, but since the coefficients p_1, p_2 and p_3 in (7) and (8) are time-dependent, some modification of the usual algorithm (Roache 1976) for solution of the equations in this form is necessary. At each timestep the sequence of operations is as follows:

(1) Update ζ at internal points and the outflow boundary.
(2) Update coefficients p_1, p_2, p_3 and p_4.
(3) Update ψ on the boundaries.
(4) Solve Poisson-type equation for ψ at internal points.
(5) Update ζ at the walls.

Note that ζ at internal points is updated prior to the updating of the coefficients, because a leapfrog finite-difference scheme is used to represent the vorticity transport equation, and the coefficients and derivatives on the right-hand side of (7) are thus evaluated at the same time level.

The problem was to be solved using a CYBER 205 computer incorporating vector processing, and this fact influenced the choices of numerical methods. Hence an explicit scheme was chosen to update the vorticity field, in preference to the ADI approach, since the inversion of the tridiagonal matrix which is required in the latter case is not readily vectorizable. An additional argument against the use of ADI methods in the present case is the fact that a scheme accurate to second order in the timestep size cannot be found for equations in which there is a cross-derivative term (McKee & Mitchell 1970); such a term is present in (7) because of the form (9) for $\nabla^2\zeta$. Thus a mid-point leapfrog scheme was adopted, with central second-order differences throughout with equal increments in x and z, and using the Dufort–Frankel substitution (Roache 1976, p. 61). The finite-difference expression used to update ζ at each timestep is given in the Appendix.

3.2. *The Poisson equation for the stream function*

Equation (8) was represented by second-order central differences, and the resulting finite-difference equations (see Appendix) solved by relaxation methods, using the multigrid strategy given as 'Cycle C' in Brandt (1977). Each sweep was carried out by Jacobi relaxation, with under-relaxation factor 0.8. The parameters governing switches to coarser and finer meshes took the values $\eta = 0.625$ and $\delta = 0.219$ in Brandt's notation, with unweighted injection of fine-mesh residuals and linear interpolation of coarse-mesh corrections. The common mesh-size ratio was 2. Overall convergence was determined by the size of the maximum residual on the finest grid, which was required to be less than $0.1 \times h^4$, where h was the finest mesh spacing.

3.3. *Boundary conditions*

The Woods expression for wall vorticity was utilized (Roache 1976, p. 141), although modification of the usual form was necessary because of the transformation (6) and the fact that the wall at $z = 0$ is moving. The finite-difference expressions for wall vorticity, which are accurate to order h^2, are given in the Appendix (A 13 and A 14). The stream function was held constant at a value of unity on $z = 1$, whilst on $z = 0$ equation (20) was utilized, with an analytic expression for the integral evaluated at each node.

The outflow boundary condition of parallel flow at infinity was of necessity replaced by conditions on the derivatives of ψ and ζ at the computational boundary. ψ at outflow was obtained by solving, at each timestep, the tridiagonal system resulting from a neglect of the axial derivative in (8) (p_2 being indentically zero at the outflow boundary). The vorticity was found by assuming the third derivative of ζ with respect to x to be zero at each node adjacent to the outlet boundary: a first-order-accurate finite-difference representation of this derivative leads to the extrapolation formula given in the Appendix (A 15). At inlet, a Poiseuille form was imposed on the vorticity, and ψ was again obtained by solving a tridiagonal system (once only), the axial derivative in ψ having been neglected.

The effects of imposing these boundary conditions artificially close to the moving indentation was assessed by varying the positions of the computational boundaries, and a discussion of the results of these changes is given in the next subsection.

3.4. *Accuracy and stability*

A Taylor expansion of (A 1) shows the error terms to be of orders

$$\frac{1}{St}h^2, \quad \frac{1}{\alpha^2}h^2, \quad \left(\frac{k}{h}\right)^2 \frac{1}{\alpha^2}, \quad k^2,$$

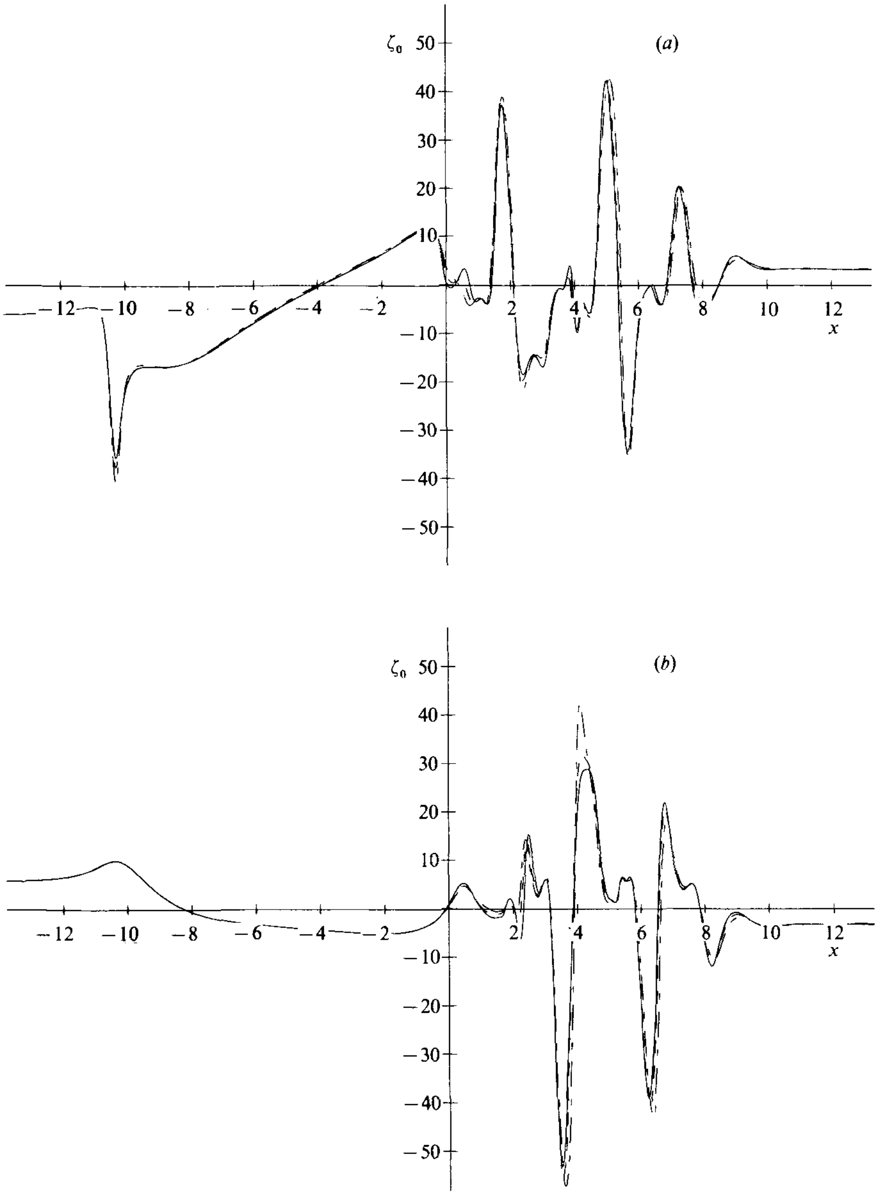

FIGURE 2. The effects of mesh size on wall vorticity plots, at $t = 0.75$ in case II: (*a*) lower wall; (*b*) upper wall. Solid curves are for $h = \frac{1}{48}$, uniform dashed curves for $h = \frac{1}{32}$ and non-uniform dashed curves for $h = \frac{1}{24}$.

where k is the timestep size. The third term arises because of the Dufort–Frankel substitution, and although at first sight may appear to be the most important, the size of the timestep required for stability is so small that this is not the case. The orders of error are, in fact, given in decreasing order of size for typical calculations, with the first error being $O(Re)$ greater than the next. Thus, in the high-Reynolds-number flows of interest, the dominant error is of order $(1/St)\,h^2$.

Numerical tests have thus concentrated on varying h, with k determined by stability considerations. Figure 2 shows sample wall-vorticity plots obtained with

			Spatial and temporal increments					
	Re	*St*	*h*	*k*	*h*	*k*	*h*	*k*
Case I	507	0.037	1/24	1/3200	1/32	1/4000	1/48	1/6000
Case II	600	0.057	1/24	1/3200	1/32	1/4000	1/48	1/6000
Case III	670	0.019	1/24	1/6000	1/32	1/10000	1/48	1/20000

TABLE 1. Flow parameters of the cases studied

	Case I			Case II			Case III		
t	$h=\frac{1}{24}$	$h=\frac{1}{32}$	$h=\frac{1}{48}$	$h=\frac{1}{24}$	$h=\frac{1}{32}$	$h=\frac{1}{48}$	$h=\frac{1}{24}$	$h=\frac{1}{32}$	$h=\frac{1}{48}$
0.1	13.00	12.99	12.97	18.49	18.48	18.45	9.96	9.97	9.96
0.2	19.52	19.52	19.52	28.23	28.20	28.17	14.62	14.63	14.64
0.3	25.13	25.12	25.11	35.12	35.12	35.13	19.48	19.51	19.53
0.4	25.07	25.07	25.06	31.82	31.81	31.82	21.20	21.20	21.21
0.5	16.07	16.07	16.07	15.44	15.44	15.45	16.61	16.61	16.61
0.6	18.76	19.06	19.43	42.95	41.27	42.67	13.23	13.35	13.50
0.7	19.96	19.92	20.08	55.44	43.87	39.70	11.37	11.37	11.41
0.8	16.72	16.56	16.47	34.43	28.18	28.96	8.91	8.92	8.95
0.9	15.05	15.12	15.17	31.74	32.43	31.64	7.15	7.10	7.07
1.0	13.33	13.48	13.61	29.63	29.57	28.48	7.97	7.98	8.00

TABLE 2. Quantitative assessment of the effects of mesh size on solutions: values of the maximum vorticity on the upper wall (for $-1.25 < x < 11.25$) as a function of time and mesh size, for flow cases I, II and III

three different values of $h(\frac{1}{24}, \frac{1}{32}$ and $\frac{1}{48})$ for one of the flows considered in detail (case II, see table 1). The present concern is with the apparent convergence of the scheme as h decreases, and it can be seen that there is indeed close correspondence of the graphs for $h = \frac{1}{32}$ and $\frac{1}{48}$, whilst the results for the coarsest mesh show qualitatively very similar features. The time $t = 0.75$ was chosen as a 'worst case' to illustrate the dependence on mesh size since the wave which is generated downstream of the indentation has, by this time, given rise to a complex vorticity distribution: at earlier and later times in the cycle there is even less dependence of vorticity on mesh size. For cases I and III similar comparisons of wall-vorticity plots were made for a number of values of h and the agreement was as good as or better than that in case II. It can be seen from figure 2 that a sensitive measure of the mesh-size dependence is the variation with mesh size of the maximum value of vorticity at the wall (the unindented wall, say) $\zeta_{\max}$, and values of $\zeta_{\max}$ for cases I, II and III, at various times in the flow cycle and for different values of h are given in table 2. The agreement of $\zeta_{\max}$ for the finer meshes suggests that the quantitative accuracy of the numerical results is quite good. Finally, it should be stated that there is a correspondingly close similarity between streamline plots obtained for different mesh sizes.

The effects on the solution of applying the up- and downstream boundary

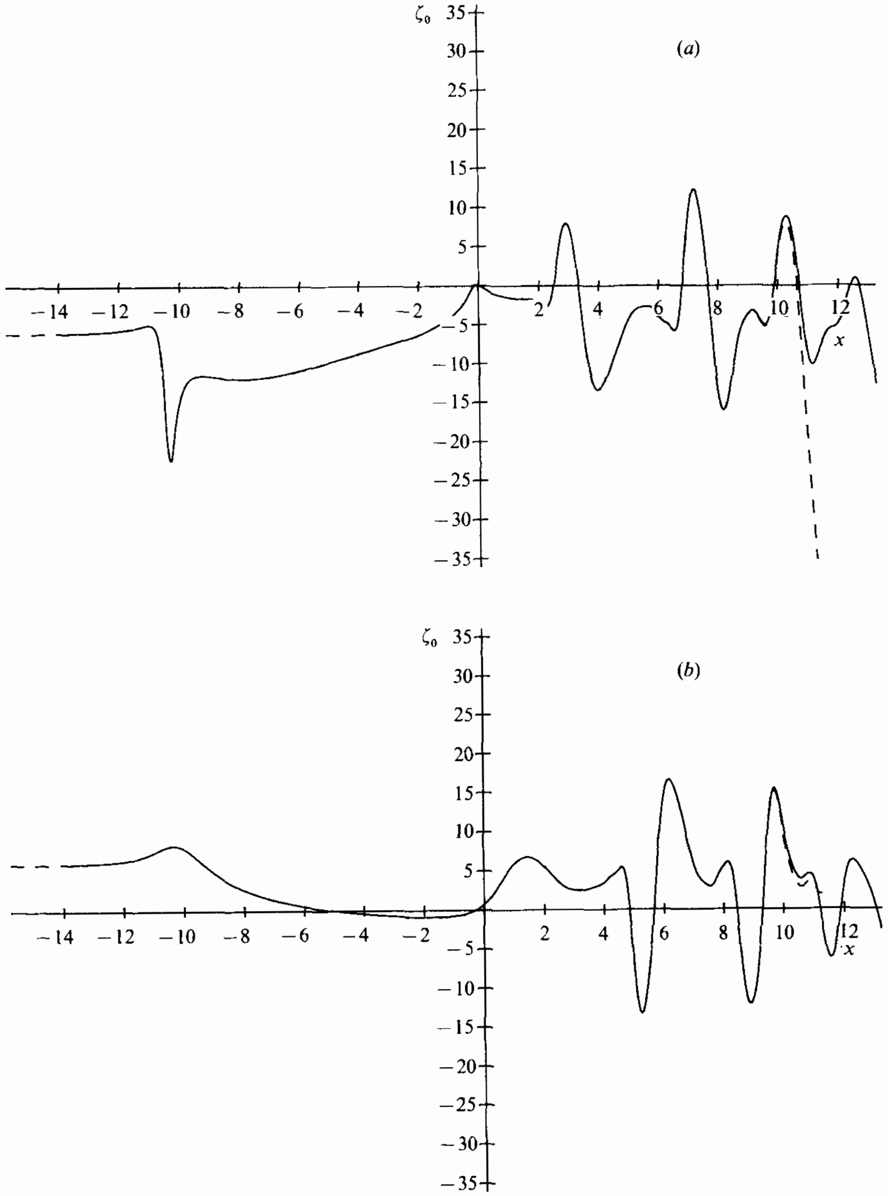

FIGURE 3. The effects of artificial numerical boundary conditions on wall vorticity plots at $t = 0.80$ in case I: (*a*) lower wall; (*b*) upper wall. Solid curves are for $(x_2 - x_1) = 2$, $(x_6 - x_5) = 12$, dashed curves are for $(x_2 - x_1) = 4$, $(x_6 - x_5) = 10$.

conditions at finite distances from the indentation have also been considered. In figure 3 are plotted the wall vorticity variations for case I (with $h = \frac{1}{32}$) for two pairs of values of x_1 and x_6: $x_1 = -13.75$, $x_6 = 13.25$ (solid curve) and $x_1 = -15.75$, $x_6 = 11.25$ (dashed curve). It can be seen that the curves are coincident to within the accuracy of the plotting, except near the outlet boundary of the second configuration. Results given below are for the first configuration, and we expect, therefore, that solutions are not affected by the downstream boundary condition for $(x_6 - x) > 2$.

The effect of the boundary condition at the entrance to the flow region is of less concern (since we are primarily interested in the region $x > x_4$), but is seen to be small, even near the entrance.

The limitation on the size of the timestep for the leapfrog method with the Dufort–Frankel substitution has been shown by Schumann (1975) to be somewhat more restrictive than the simple CFL criterion predicted from a one-dimensional analysis. In the present problem stable values of k have been found empirically and are given in table 1. The c.p.u. time required to compute a complete cycle of the flow varied between about 100 s for $h = \frac{1}{24}$ (about 15000 nodes) and 1000–2000 s for $h = \frac{1}{48}$ (about 60000 nodes) on the CYBER 205. Note that in each case only a single cycle has been computed, since the residual perturbation of the velocity field at the end of a cycle is small and unlikely to affect significantly the subsequent development of the flow. Furthermore, the experiments show that three-dimensional instabilities grow rapidly during the last stages of the cycle, so that it is not clear that a two-dimensional simulation would agree more closely with experimental results if the transient effect were eliminated by computing a number of cycles.

4. Description of results

Results were obtained for three pairs of values of Reynolds number and Strouhal number as given in table 1. These parameters are the same as in certain of the flows considered experimentally and theoretically in PS, allowing quantitative comparison of various flow features. The amplitude of the wall movement, $\epsilon = 0.38$, is the same in each case. Qualitative comparison of instantaneous streamline plots with the photographs of PS is also possible, since the exposure times for the photographs are short compared with the timescale for changes in the velocity field, and thus the particle paths, appearing as short streaks, are approximately coincident with the streamlines.

4.1. *Flow I – development of wave*

Figure 4 shows instantaneous streamline plots for flow case I, obtained using the mesh with $h = \frac{1}{32}$. The values of stream function for which contours were plotted, were chosen according to the following scheme:

$$\psi_c = \psi_w + \tfrac{1}{6}(i-1)(1-\psi_w), \quad i = 1, 7, \tag{23}$$

$$\psi_c = 1 + \tfrac{1}{4}i(\psi_{max} - 1), \quad i = 1, 3, \tag{24}$$

and

$$\psi_c = \psi_w + \tfrac{1}{4}i(\psi_{min} - \psi_w), \quad i = 1, 3, \tag{25}$$

where ψ_w was the stream-function value at the indented wall for $x > x_5$ and ψ_{max} and ψ_{min} were the maximum and minimum values of the stream function in the range of x shown. The caption gives values of ψ_w, ψ_{max} and ψ_{min}.

The flow development is essentially the same as that found by PS, and is summarized only briefly here. At some time between $t = 0.2$ and $t = 0.25$, separation occurs in the lee of the indentation, and the resulting eddy grows rapidly (figure 4*b, c*). A second eddy, of opposite sign, forms on the upper wall some distance downstream of the first, a third appears still further downstream on the lower wall (figure 4*d*), and so on until there is a sequence of such eddies, of alternating sign, bounded by a wavy core flow (figure 4*g*). We shall adopt the convention of SPLS and PS in labelling the eddies alphabetically, as shown in figure 4*g*: it can be seen that eddy B splits into two parts between $t = 0.60$ and $t = 0.65$. As t increases, not only

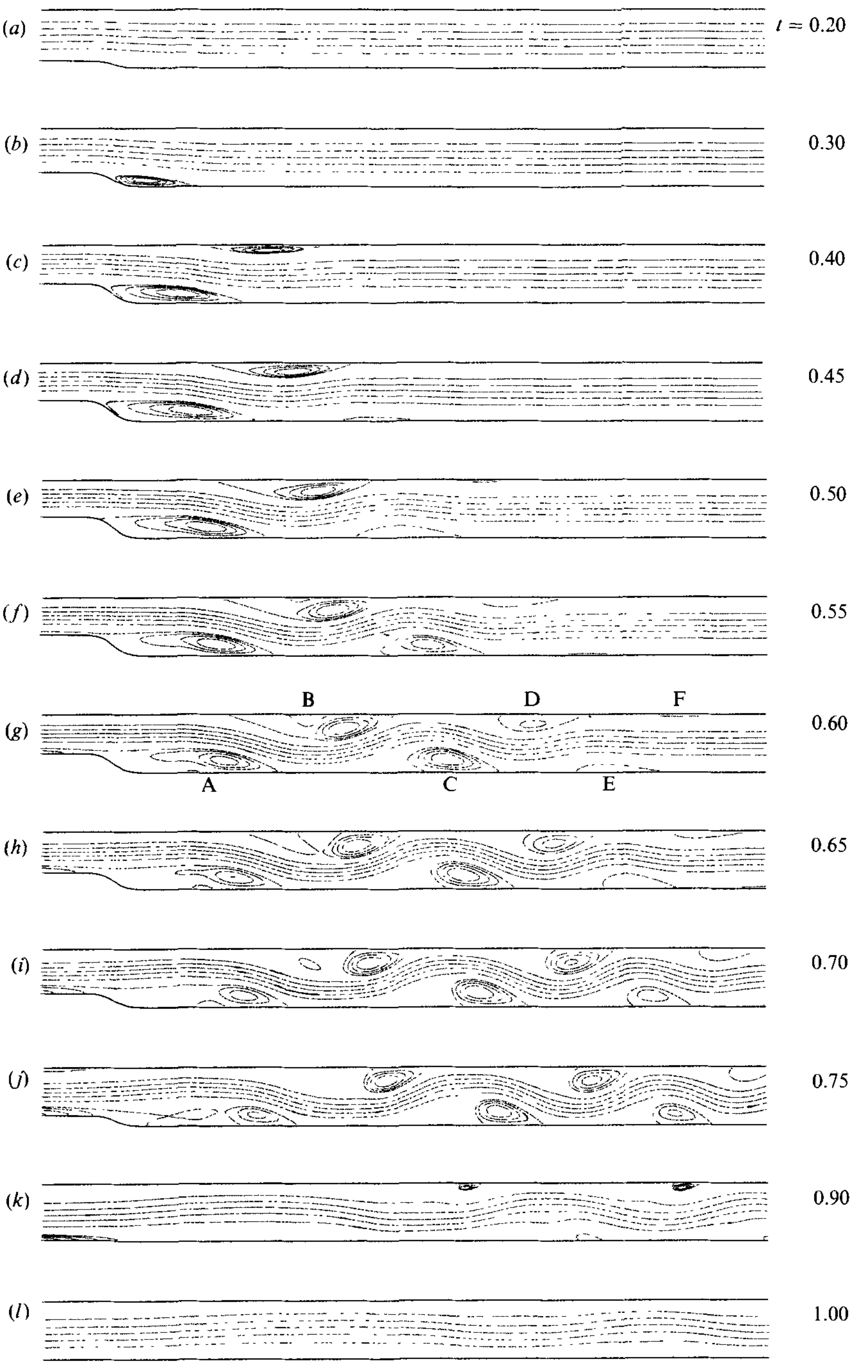

FIGURE 4. Instantaneous streamline plots for case I: (*a*) $\psi_{\max} = 1.000$, $\psi_{\min} = -0.441$, $\psi_w = -0.441$; (*b*) 1.000, −0.456, −0.441; (*c*) 1.009, −0.326, −0.273; (*d*) 1.037, −0.215, −0.143; (*e*) 1.076, −0.081, 0.000; (*f*) 1.101, 0.060, 0.143; (*g*) 1.109, 0.185, 0.273; (*h*) 1.106, 0.280, 0.375; (*i*) 1.093, 0.354, 0.441; (*j*) 1.072, 0.394, 0.464; (*k*) 1.003, 0.240, 0.273; (*l*) 1.000, 0, 0.

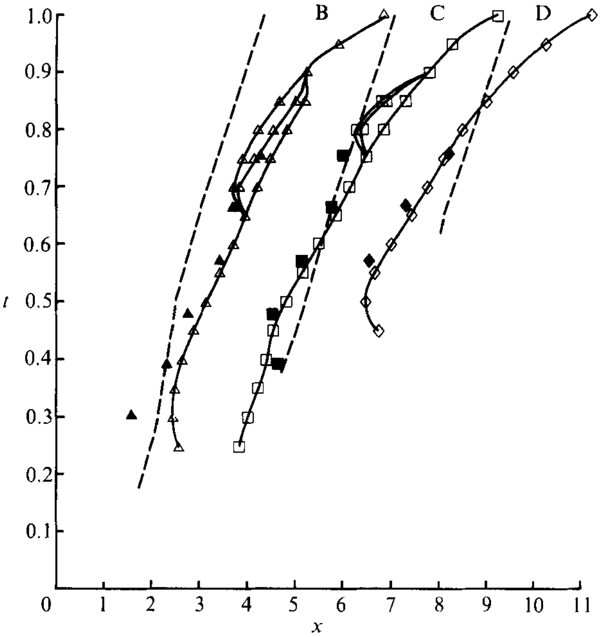

FIGURE 5. Positions of crests and troughs corresponding to eddy B (triangle symbols), eddy C (square symbols) and eddy D (diamond symbols) in case 1. Filled symbols show experimental results from PS, unfilled symbols joined by unbroken lines are numerical results from the present work. Results from the small-amplitude, inviscid theory of PS are shown as broken lines.

does the number of eddies increase, but the lateral extent of existing eddies and the amplitude of the core's waviness also increases. The speed at which the wave front propagates (the group velocity) is considerably greater than the speed at which an individual crest or trough travels (the phase velocity). The eddies downstream of eddy B do not double in this computation, in contrast to figure 5 of PS, where C also doubled but *Re* was a little larger than here: 610 not 507. As the indentation recedes late in the cycle, the eddies shrink in size and strength and are swept downstream (figure 4*k*, *l*). A region of flow reversal is briefly formed on the upper wall opposite the indentation (figure 4*j*), but at $t = 1.0$ (figure 4*k*) there is again vorticity of uniform sign at each wall.

The group velocity and the phase velocities of different crests/troughs have been estimated from the time-variation of the stream function in the flow. Wave-crest positions as functions of time were obtained from the turning points in the axial variation of the stream function at the centreline of the channel. The locations of the turning points corresponding to eddies B, C and D are plotted as unfilled symbols joined by unbroken lines in figure 5. When eddy doubling, or its precursor, streamline kinking, occurs, there may be three turning points corresponding to a single eddy, and this is shown in figure 5 by trifurcation of the unbroken lines. Phase velocities for B, C and D can be estimated from the numerical values of $\mathrm{d}x/\mathrm{d}t$ in figure 5, which must be multiplied by the Strouhal number in order to obtain velocities scaled on $\hat{U}_0$; the resultant scaled phase velocities are approximately 0.2, 0.3 and 0.4 respectively. The filled symbols represent experimental results from PS, which are discussed below. The broken curves represent the predictions of the small-amplitude theory developed in SPLS and PS.

The group velocity has been estimated by calculating the differences, $\Delta\psi$, between

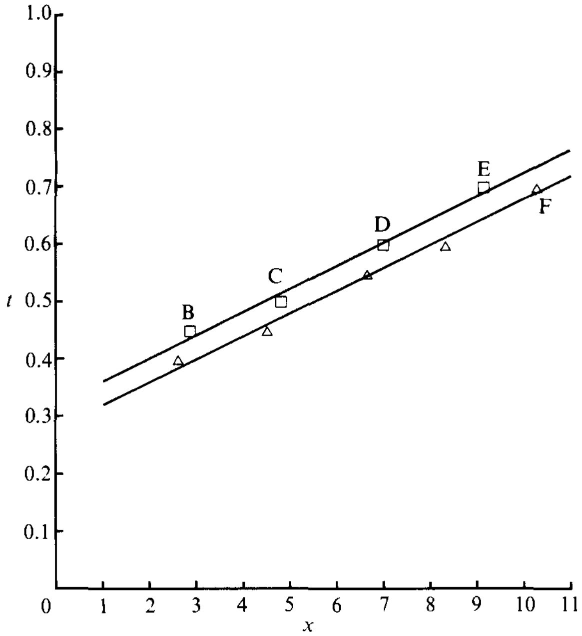

FIGURE 6. Values of t at which $\Delta\psi$ for each of eddies B to F attains the magnitudes 0.05 (triangle symbols) and 0.15 (square symbols), versus the axial locations of the eddy crests/troughs at these times.

the turning values of the stream function at the centreline and the centreline value for parallel flow. In figure 6, the times at which $\Delta\psi$ for each of eddies B to F first attains a threshold value, $\Delta\psi_0$, are plotted against the axial locations of the eddy crests/troughs at these times. Figure 6 therefore shows the time required for a given magnitude of disturbance to propagate a given distance, and is thus a measure of the group velocity. Two arbitrary values of $\Delta\psi_0$ are considered, 0.05 and 0.15, giving approximate values of $\mathrm{d}x/\mathrm{d}t$ of 25.2 and 24.6 respectively; the difference between these values is probably attributable to the finite time-resolution of the results. Multiplication by St gives the values 0.93 and 0.91, which compare favourably with the experimentally determined group velocity of about 1.0, obtained from figure 10 of PS. Since the mean fluid velocity is unity, these estimates of group velocity are consistent with the idea that the wave front is propagated primarily by convection within the core of the fluid rather than in slower-moving boundary layers. We note that the phase velocities of individual crests/troughs are smaller than the group velocity by factors of between about 2.3 and 4.6.

4.2. *Flow I – eddy doubling*

The mechanism responsible for the splitting of eddies A and B, each into a pair of corotating recirculations, is of considerable interest (see PS); the sequence of events can be examined in more detail in the numerical simulation than is possible experimentally, although qualitatively the streamline plots agree well with figure 5 of PS, despite the larger Reynolds number of 610 in that case. Concentrating on eddy B from its formation (figure 4*c* here, 5*b* of PS), we see that initially the closed streamlines are fairly symmetrical about the eddy centre. Later, they become more concentrated near the reattachment point (figure 4*e* here, 5*c*, *d* of PS), and subsequently a secondary, counter-rotating separation region forms (figure 4*f*). The secondary eddy grows and the primary dividing streamline becomes kinked (figure 4*g*), until primary and secondary streamlines meet and give a pair of corotating eddies (figure 4*h* here, 5*e* of PS). It is possible that a local stream-function minimum is still present in figure 4(*h*), located between the corotating parts of eddy B, but it does not appear owing to the automatic contour-value selection. The corotating eddy becomes detached from the wall (figure 4*i*) and then disappears (figure 4*j*).

A similar sequence of events may be inferred for eddy A: it appears that a detached corotating recirculation is about to be formed at $t = 0.65$. However it is weak and fails to be captured by the plotting routine at $t = 0.70$, although it is just captured at $t = 0.75$. Doubling of eddy A has not previously been reported, although on careful examination, figure 4(*d*, *e*, *f*) of PS appears to be consistent with such an occurrence. For eddies other than A and B, no secondary separation is found numerically, but we do note the concentration of streamlines at the downstream part of a given eddy and the development of kinked streamlines near eddy C (figure 4*i*, *j*).

With the aim of achieving a better understanding of the physical mechanisms underlying eddy doubling, vorticity contours have been plotted, and those corresponding to flow case I are given in figure 7. Contour values, ζ_c, were chosen according to

$$\zeta_c = \tfrac{1}{8}(i-1)\,\zeta_{\max}, \quad i = 1, 8, \tag{26}$$

$$\zeta_c = \tfrac{1}{8}i\,\zeta_{\min}, \quad i = 1, 7, \tag{27}$$

where $\zeta_{\max}$ and $\zeta_{\min}$ were the instantaneous maximum and minimum values of vorticity in the region shown.

At early times in the cycle, the vorticity contours are approximately parallel with the channel walls, and are closer together near the walls than at the centre of the channel. This is because the flow is accelerating and vorticity is being generated at the walls more rapidly than it can diffuse away from them. Subsequently, the vorticity contours become wavy and, in the core region, are almost coincident with the streamlines, confirming that vorticity transport is primarily convective in this part of the flow. The eddy core is represented by a region of approximately uniform vorticity (blank in figure 7) which is convected to a position at the downstream end of each eddy (see figure 7*e*+ for eddy B, figure 7*f*+ for eddy C etc.). Because of the no-slip condition, vorticity of opposite sign is generated between the core of each eddy and the wall. This is convected around the eddy, first upstream, then towards the centre of the channel, and then downstream again. As diffusive (viscous) cancellation with the vorticity of the main part of the eddy occurs, a characteristic 'comma'-shaped contour is produced. In the case of eddy B, the tail of the comma is broken (figure 7*g*, *h*), giving rise to a closed vorticity contour. We identify the above process with eddy doubling.

Thus, although the wave generation process and the formation of the principal region of closed streamlines in the eddy are essentially inviscid consequences of the distortion of the oncoming vorticity profile, viscosity is an essential factor in eddy doubling, both in the generation of counter-vorticity beneath the main eddy and in the diffusion of vorticity that leads to contour breaking later on (though not in the advection of the countervorticity around the primary vortex). We believe that this description of the vorticity dynamics gives a more soundly based account of eddy doubling than other explanations that have been offered. For example, Tutty & Cowley (1986) suggested that eddy doubling may be the result of a linear Rayleigh instability of the unsteady boundary-layer velocity profiles (such instabilities were

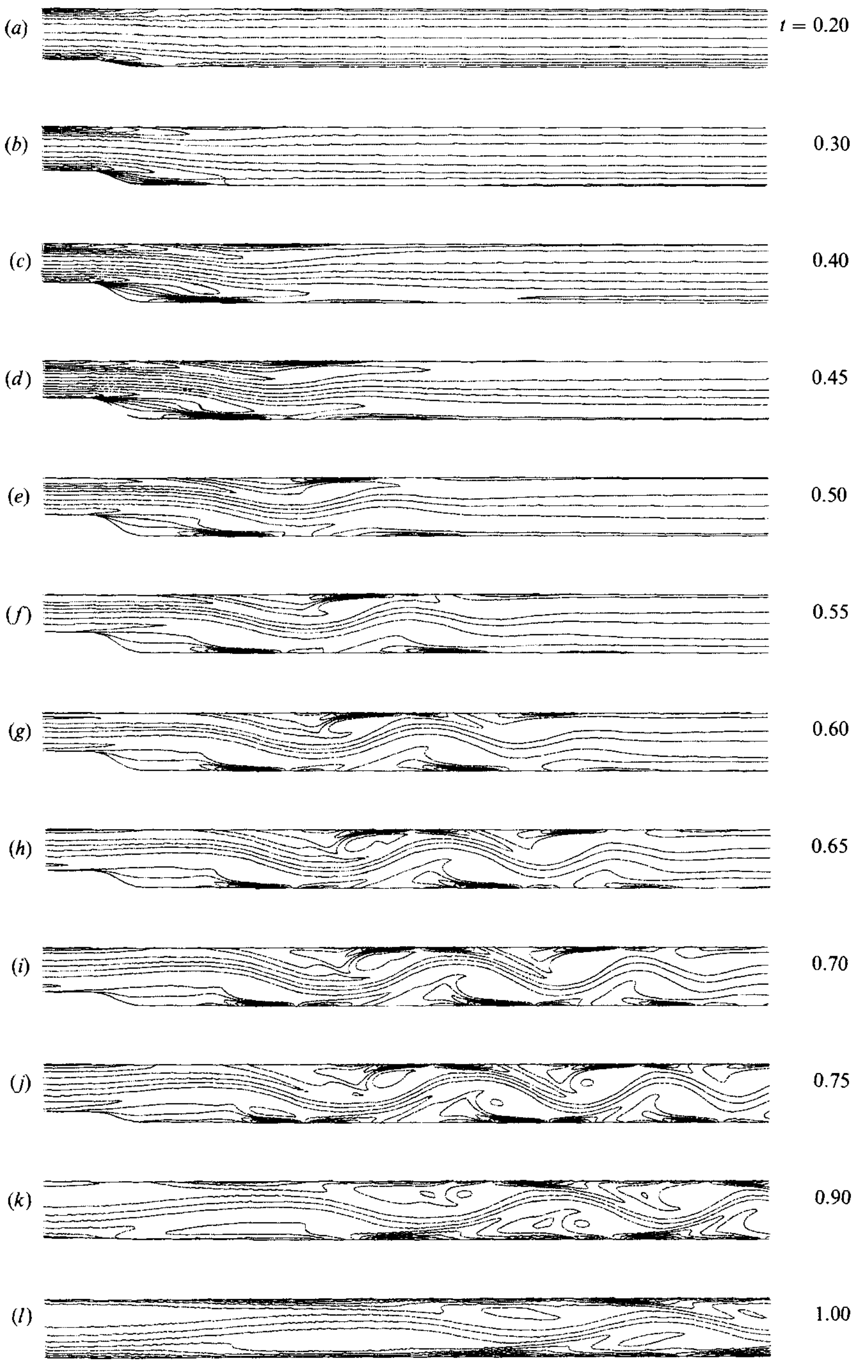

FIGURE 7. Instantaneous vorticity contour plots for case I: (*a*) $\zeta_{max} = 19.5$, $\zeta_{min} = -15.3$; (*b*) 25.1, −17.8; (*c*) 25.1, −17.2; (*d*) 24.4, −16.4; (*e*) 26.1, −27.4; (*f*) 25.5, −33.2; (*g*) 24.0, −31.5; (*h*) 23.0, −27.9; (*i*) 19.9, −23.6; (*j*) 17.9, −18.7; (*k*) 15.1, −14.5; (*l*) 13.5, −13.2.

first investigated, in the context of steady, interactive boundary-layer calculations, by Smith & Bodonyi 1985). However, the experiments show the phenomenon to be deterministic and reproducible (PS), and furthermore it is not clear that the assumption of parallel flow is justified near the wall in (say) eddy B. Even if the assumption is valid, figures 4 and 7 show that Rayleigh's and Fjortoft's criteria for linear inviscid instability are satisfied in the vicinity of eddy B from as early as $t = 0.4$, after which one would expect a very rapid growth of the instability, whereas eddy doubling does not occur until $t = 0.65$, by which time the vorticity contours have been grossly modified by nonlinear effects.

The idea that eddy doubling may occur through a non-linear, inviscid wave-breaking process has been discussed by Borgas (1986), and there is evidence that the nonlinear vorticity dynamics play an important role: indeed the vorticity plots of figure 8 show features strikingly similar to those of Dritschel (1988), obtained using the inviscid methods of contour dynamics. Borgas argues that, for a thin eddy, significant irreversible distortion of vorticity contours occurs in a finite time only when the eddy is bounded by a strong vortex sheet: although there is no evidence of the latter in our computations, neither is the eddy thin compared with the channel width. Borgas proposes, as an alternative mechanism, that backwards wave breaking of the kind described by Stern & Pratt (1985) may cause eddy splitting. However, if this process were to occur, the sense of rotation of an eddy before splitting would need to be counter-clockwise on the lower wall or clockwise on the upper wall, opposite to the sense observed.

Yet another potential mechanism of eddy doubling, also briefly discussed in PS and suggested by F. T. Smith, relates it to the ejection into the flow of bursts of vorticity from the neighbourhood of the point of breakaway separation at the upstream end of the eddy (cf. Smith & Burggraf 1985). According to this idea the main region of closed streamlines consists of one such burst, formed early in the wave generation process and convected to the downstream end of the eddy. Behind this would be a relatively thin vortex sheet, and the second, corotating eddy forms either because this becomes unstable and rolls up or because of the ejection of another burst from the separation point. The present results suggest that this mechanism is not dominant in the case of eddy B, because there is no evidence of either a vortex sheet or a significant concentration of vorticity emerging from the separation point just prior to eddy doubling. On the other hand, the additional covorticity which is generated at the wall above eddy A, upstream of eddy B just before it doubles, presumably contributes to the development of the new corotating eddy, although stronger regions of locally enhanced covorticity are also present upstream of eddies C to F without giving rise to doubling (see also figures 8, 9). Some recently computed solutions of the Euler equations for the same time-dependent geometry (M. E. Ralph & T. J. Pedley, in preparation) show that eddies of comparable strength to those found here are also formed beneath the wave crests in inviscid flow. However, the eddies are shorter in an inviscid fluid, and eddy doubling does not occur, so viscosity clearly has an important effect on the development of the eddies. Whether burst ejection makes a significant contribution cannot yet be determined for this case.

4.3. *Flow I – wall vorticity*

Further aspects of the flow are revealed by plots of wall vorticity ζ_0, and those corresponding to the streamline plots of figure 4 are given in figures 8 and 9 for the upper (unindented) and lower (indented) walls respectively. In figure 8, negative values of ζ_0 correspond to reversed wall shear, whilst positive values show flow

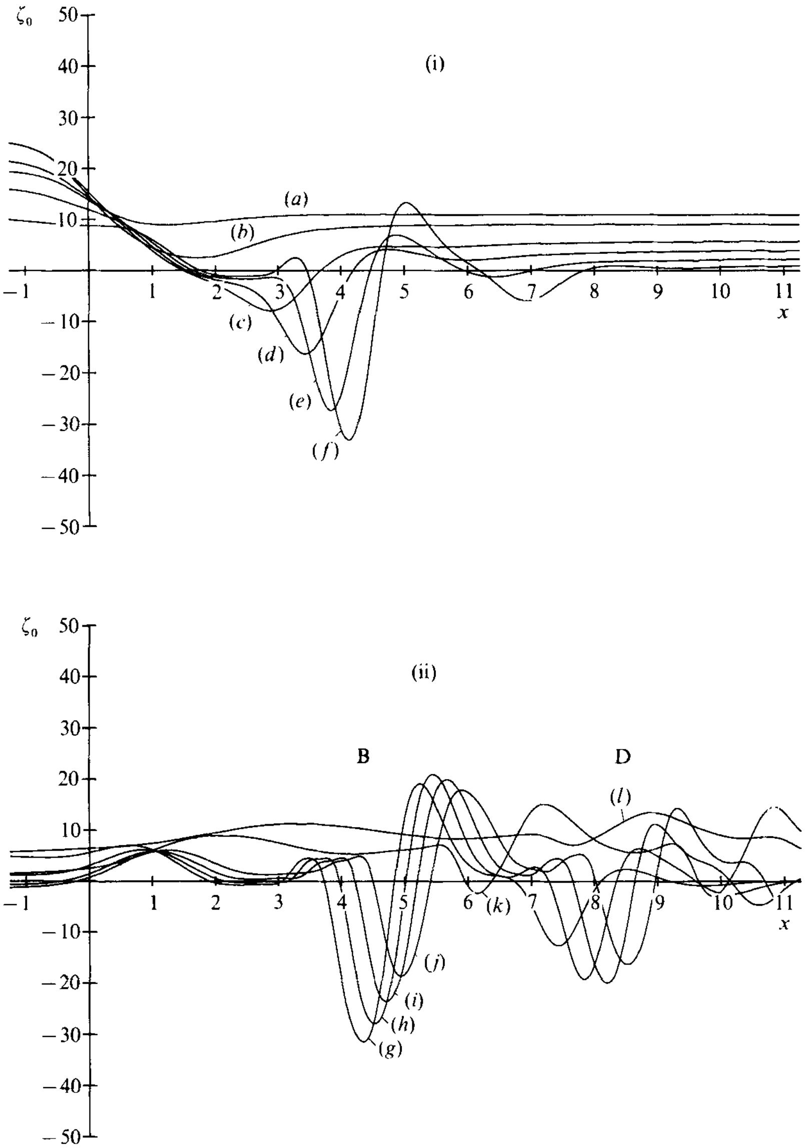

FIGURE 8. Vorticity variation at the upper wall in case 1: (*a*) $t = 0.20$; (*b*) 0.30; (*c*) 0.40; (*d*) 0.45; (*e*) 0.50; (*f*) 0.55; (*g*) 0.60; (*h*) 0.65; (*i*) 0.70; (*j*) 0.75; (*k*) 0.90; (*l*) 1.00.

reversal in figure 9. We can trace the development of eddy B, for example, in figure 8. A local minimum in ζ_0 is seen to develop initially near $x = 1.5$ (curves *a* and *b*) which leads to flow reversal at the wall and a local change in the sign of ζ_0 (curve *c*). Already, the minimum of ζ_0 is nearer the downstream end of the region of separation, and this effect becomes increasingly pronounced. At $t = 0.50$ (curve *e*) two distinct regions can be identified: an upstream zone in which there is a small, almost uniform value of ζ_0, and a downstream zone with a large and nearly symmetrical extremum. As this becomes greater in magnitude, it moves downstream more rapidly than the position of the wave crest, roughly midway between the separation and reattachment points. The development of a large (negative) peak in wall vorticity and its

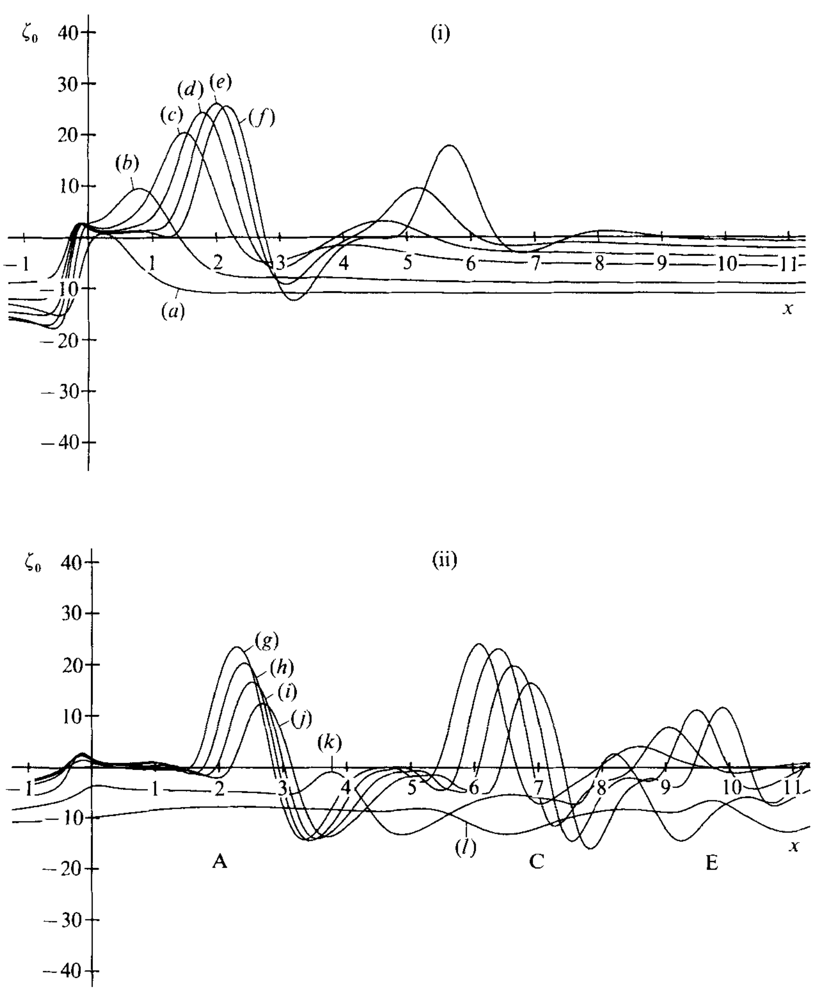

FIGURE 9. Vorticity variation at the lower wall in case I: (*a*) $t = 0.20$; (*b*) 0.30; (*c*) 0.40; (*d*) 0.45; (*e*) 0.50; (*f*) 0.55; (*g*) 0.60; (*h*) 0.65; (*i*) 0.70; (*j*) 0.75; (*k*) 0.90; (*l*) 1.00.

downstream movement correspond to the concentration of closed streamlines near the reattachment point of the eddy.

Next, a small embedded region of positive vorticity develops within eddy B (curve f), the two distinct regions of negative vorticity corresponding to the two corotating eddies resulting from eddy doubling. Subsequently, the sign of the vorticity in the upstream part of the eddy becomes positive again (curves g and h), but the local maximum in ζ_0 persists until the end of the flow cycle. The minimum of ζ_0 corresponding to the core of eddy B begins to decrease in magnitude (curves 8g–k) as it continues to move downstream, until at $t = 1.00$ (curve l) the wall vorticity has uniform sign and only small spatial variations.

Figures 8 and 9 also show that the development of eddies C, D and E follow a similar course to that of eddy B, with two exceptions. First, there are zones of markedly increased positive vorticity just upstream of eddy D (figure 8) and of negative vorticity upstream of eddies C and E (figure 9), corresponding to the wave crest above eddy C and the troughs below eddies B and D (cf. figure 7). Secondly, in

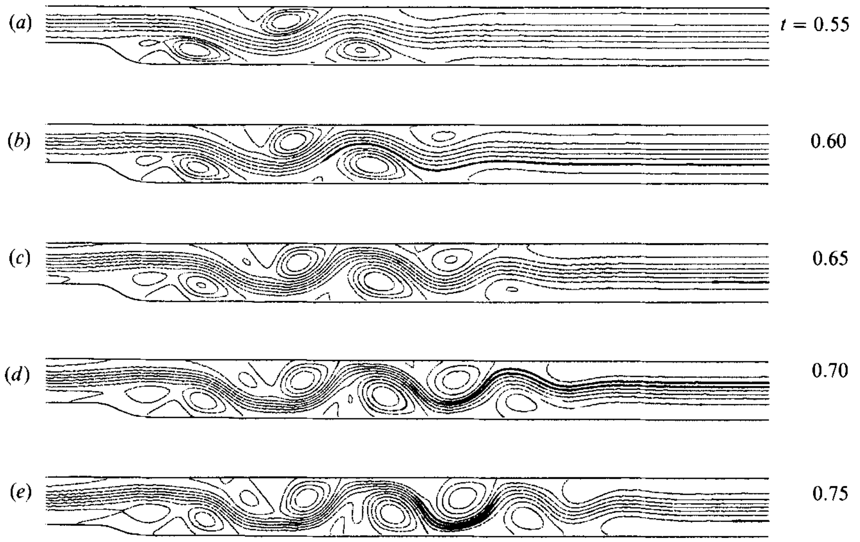

FIGURE 10. Instantaneous streamline plots for case II: (*a*) $\psi_{max} = 1.221$, $\psi_{min} = 0.058$, $\psi_w = 0.221$; (*b*) 1.252, 0.225, 0.420; (*c*) 1.268, 0.355, 0.578; (*d*) 1.271, 0.461, 0.680; (*e*) 1.252, 0.515, 0.715.

the region of nearly uniform wall vorticity upstream of the peak in $|\zeta_0|$, the sign of ζ_0 does not change. Nevertheless, a local turning point of opposite sign develops just upstream of the primary extremum in each case, as for eddy B. Furthermore, the time interval between the first occurrence of separation associated with an eddy and the formation of the corresponding opposite extremum in wall vorticity is approximately the same, about 0.10, for each of eddies B, C, D and E, allowing for the finite time-resolution of the results. Likewise, the interval between first separation and the attainment of the greatest wall vorticity peak is about 0.15 in each case. (Compare figure 8 curves *c*, *e*, *f* for eddy B; 9*d*, *f*, *g* for eddy C; 8*e*, *g*, *h* for eddy D; and 9*f*, *h*, *i* for eddy E.) These similarities suggest that the eddies have essentially identical structure, apart from the decrease in magnitude of peak $|\zeta_0|$ with distance downstream. We note, however, that eddy A, whose inception is quasi-steady, does not show the same development.

4.4. *Flows II and III*

The principal features of flow II, with higher values of *Re* and *St*, are similar to those of flow I (table 1), but certain details differ, and the streamline plots that show the differences are given in figure 10. The corresponding vorticity plots are given in figure 11. Comparison of figure 10 with figure 4 reveals that the wavelength is considerably shorter in case II. Another difference is that after eddies A and B double, the strength of recirculation of each upstream part is greater in case II than case I. Furthermore, secondary corotating eddies are seen upstream of eddies C and D in figure 10, although their formation is not apparently preceded by the occurrence of a secondary counter-rotating recirculation, embedded within the primary vortex, as is the case for eddies A and B. Plots of wall vorticity (figure 12) show that the zones of enhanced vorticity on the walls opposite the crests/troughs (e.g. of positive vorticity upstream of eddy D, opposite the crest of eddy C) are shorter and more concentrated than in case I. Thus ejection of vorticity at the separation point may play a greater role for larger values of *Re*, which would be consistent with the ideas of Smith (see §4.2

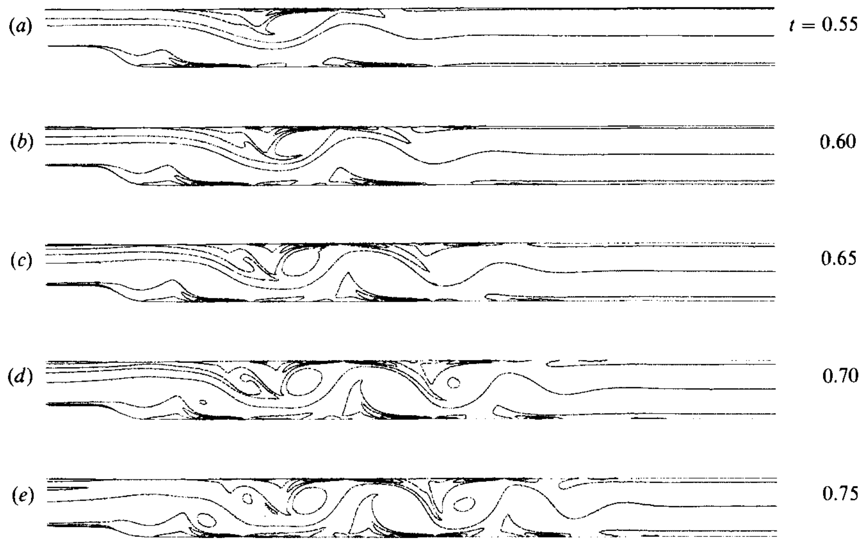

FIGURE 11. Instantaneous vorticity contour plots for case II: (a) $\zeta_{\max} = 53.2$, $\zeta_{\min} = -82.0$; (b) 53.0, −81.3; (c) 52.2, −76.3; (d) 46.1, −66.1; (e) 42.5, −55.4.

above). Distinct recirculations can be seen on figure 10 in the regions where the core flow diverges rapidly from the wall. The generation of counter-vorticity beneath the eddy core nevertheless plays a similar role in the doubling of both B and C: in the former case it is this generation process that splits a single eddy into two parts, whilst in the latter it serves to inhibit coalescence of two already distinct corotating eddies. This kind of doubling is not found in cases I and III, because in them the magnitude of the wall vorticity upstream of each of eddies C to F is somewhat smaller.

Another novel feature arises in the plots of wall vorticity for case II, as shown in figure 12. Concentrating on eddy B (figure 12ii), we see that, as in case I, a large extremum develops, corresponding to the primary region of closed streamlines, with a region of more uniform negative vorticity of smaller magnitude upstream, and a region of positive vorticity in between. What is particularly interesting about case II is that the secondary corotating and counter-rotating eddies themselves give rise to wall vorticity structures similar to that of eddy B overall, but on a smaller scale. Thus each secondary eddy has its own primary extremum near the reattachment point and a subsidiary pair of extrema near the separation point, with the result that eddy B gives rise to as many as seven turning points in wall vorticity. Case II is the case with largest values of *St* and α^2, so one might expect the vorticity dynamics to be dominated by unsteady inertia and therefore less influenced by viscosity. The present observations suggest that the same dynamics govern the subeddies in case II as govern the primary eddies. At even higher values of *St* and α^2 a cascade of breaking vorticity waves might be expected.

Flow case III, with a higher value of *Re* but lower *St* than case I, also develops waves in the core. The wavelength is greater than that in each of cases I and II, as expected from the inviscid, small-amplitude theory, and the amplitude somewhat less. The eddies are thus longer and thinner than in the other cases, but the regions of closed streamlines again become concentrated near the reattachment points. Eddy doubling, however, which occurs only for eddy B, is associated with a very weak and short-lived extremum in the stream function. In the experiments, the new

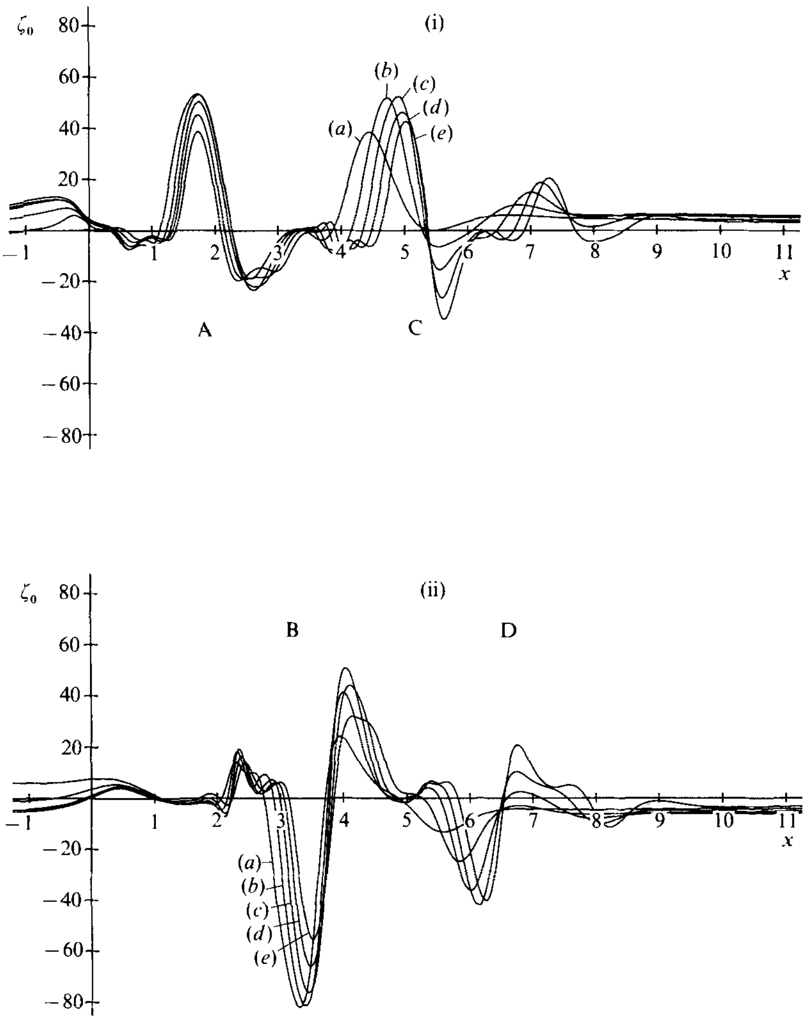

FIGURE 12. Vorticity variation at the upper (i) and lower (ii) walls in case II: (*a*) $t = 0.55$; (*b*) 0.60; (*c*) 0.65; (*d*) 0.70; (*e*) 0.75

recirculation formed by the doubling of eddy B was also observed to be weaker than in the other cases, although the difference was less marked than in the numerical solutions. Furthermore, the experiments suggested that eddy C also doubled. These discrepancies suggest that, although the effects of numerical diffusion are generally small, they may be important when the flow parameters are close to values critical for the occurrence of eddy doubling.

5. Further discussion of results and comparison with experiment

The results described in the previous section are, as already stated, in strong qualitative agreement with the experimental findings reported in SPLS and PS. In order to make a quantitative comparison between numerical and experimental results, data for the measured positions of wave crests and troughs have been taken from figures 16 and 18 of PS. These data represent axial positions at which the

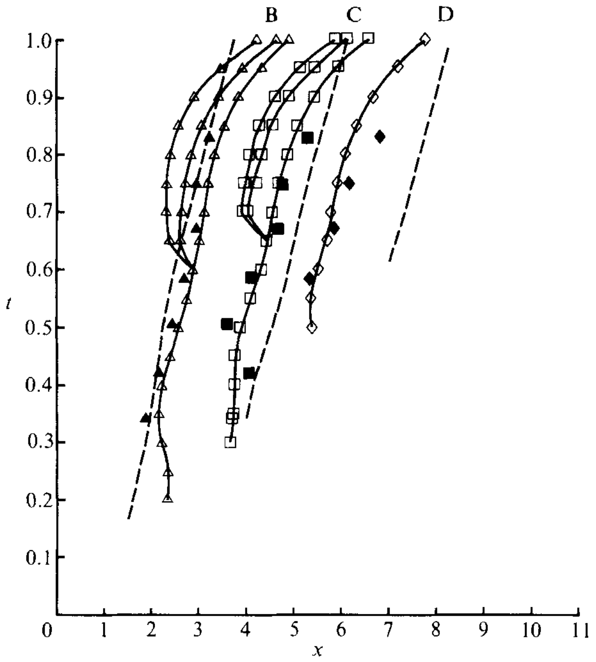

FIGURE 13. Crest and trough positions in case II (see figure 5 for explanation of symbols).

displacement of the core attained local turning values, and each extremum is identified by the same letter (B, C or D) as denotes the corresponding eddy. The x-coordinates of these turning points have been rescaled to conform to the present notation and are plotted as filled symbols in figures 5, 13 and 14. It should be noted that the displacements of different streamlines may reach maxima at slightly different axial locations, introducing an uncertainty in the experimental data. For the numerical results, a crest or trough position can be defined precisely as the axial position at which the axial stream-function variation at $y = \frac{1}{2}$ attains a turning value (see §4, above). The broken lines in figures 5, 13 and 14 have been taken from PS and show crest and trough positions predicted by the small amplitude inviscid theory.

Agreement between the numerical and experimental results shown in figures 5, 13 and 14 is generally very good, with discrepancies within the range of the experimental scatter. This gives considerable confidence in both the numerical methods and the experimental measurements, as well as demonstrating the applicability of a two-dimensional solution over most of the flow cycle. The greatest differences between the numerical and experimental results arise in figure 5, for eddy B early in the flow cycle, and in figure 13, for eddy D late in the cycle. The increased discrepancies at these points can probably be explained, in the first case, by the difficulty in determining the position of a small-amplitude crest, and, in the second case, by incipient three-dimensional effects disturbing the experiments.

The theoretical predictions of wavelength can be seen to be in quite good agreement with the numerical and experimental results. The theoretical dependence of wavelength on Strouhal number is approximately reproduced numerically, and there is therefore no reason to doubt the hypothesis of SPLS and PS that this is determined primarily by inviscid vorticity dynamics in the core. The theory predicts

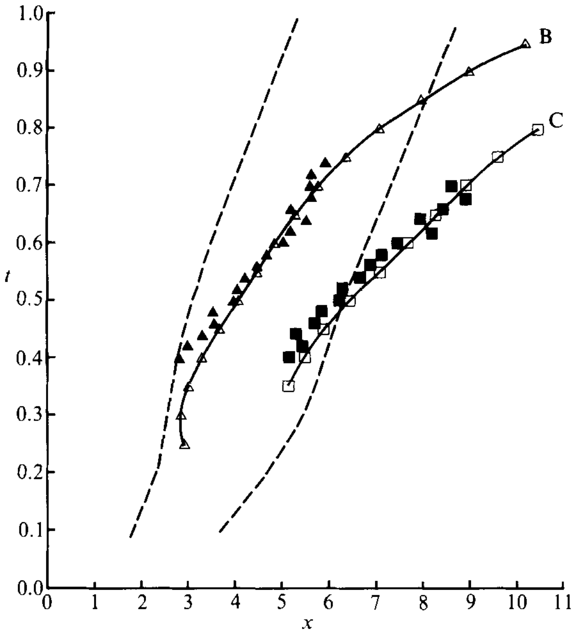

FIGURE 14. Crest and trough positions in case III (see figure 5 for explanation of symbols).

the phase velocity well in case II (highest Strouhal number), less well in case I and poorly in case III (lowest Strouhal number), and gives the position of eddy D inaccurately in all three cases. The numerical solutions of the full Navier–Stokes equations show a dramatic improvement in the prediction of these features, as expected since the assumptions of small amplitude, large wavelength and inviscid flow are not required numerically. In particular, in both the experimental and numerical flows, the flow rates downstream of the indentation incorporate large oscillatory components which may strongly affect the crest/trough positions: for example in case I the oscillatory component of flow rate has amplitude equal to approximately half the mean flow component. The small-amplitude approximation causes this feature to be neglected altogether in the theory. The question as to which of the theoretical assumptions is the most important source of error in predicting crest/trough positions is currently being investigated further. At present, the fact that agreement with experiment and numerical integration is best at the highest values of the Strouhal number suggests that, in that case, the vorticity dynamics are dominated by a balance between unsteady and convective inertia. At lower values of *St* viscous terms are needed as well to balance the convective inertia in a more quasi-steady manner.

This is not the place to go in detail into the biomedical applications of this work, but one feature of the results deserves comment in that context. There is strong evidence of a link between the initiation of atherosclerosis at sites on artery walls and the viscous shear stress at these sites, and it has been postulated that regions of flow separation are particularly vulnerable. However, much of the discussion has been based on the assumption that the wall shear in a separated eddy is *low*, as in quasi-steady flows, whereas the present results (figures 8, 9, 12) show that in unsteady flows the magnitude of the wall shear beneath an eddy can be very *high*, 5–6 times the value in steady, unseparated flow. Our results are for two-dimensional flow, but coupled with the results of Ku *et al.* (1985), which indicate that variability of wall shear stress near a time-dependent reattachment point is important, they suggest that a careful study of unsteady, internal, three-dimensional flows is needed before even a qualitative assessment of wall shear stress at particular sites in arteries can be made.

The authors wish to thank S. J. Cowley, R. D. Kamm, I. J. Sobey, K. D. Stephanoff and O. R. Tutty for useful discussions. We are especially grateful to J. W. Elliott for pointing out an error in an earlier version of this paper. The financial support of the Science and Engineering Research Council is gratefully acknowledged.

Appendix. The finite-difference equations

In the following, subscripts i and j refer to axial and transverse nodes i and j. Note that at the unindented sections of the channel the given expressions revert to simpler forms.

Denoting time level n by superscript n, the expression used to update the vorticity ζ at each timestep is as follows:

$$\begin{aligned}\zeta_{ij}^{n+1} = A_{ij}^{n}\{[1-2\gamma_1(1+a_{ij}^{n})]\,\zeta_{ij}^{n-1} &- \gamma_2 b_{ij}^{n}[(\psi_{i,j+1}^{n}-\psi_{i,j-1}^{n})(\zeta_{i+1,j}^{n}-\zeta_{i-1,j}^{n}) \\ &-(\psi_{i+1,j}^{n}-\psi_{i-1,j}^{n})(\zeta_{i,j+1}^{n}-\zeta_{i,j-1}^{n})]+\gamma_1[2(\zeta_{i+1,j}^{n}+\zeta_{i-1,j}^{n})+c_{ij}^{n}\zeta_{i,j+1}^{n}+d_{ij}^{n}\zeta_{i,j-1}^{n} \\ &+e_{ij}^{n}(\zeta_{i+1,j+1}^{n}+\zeta_{i-1,j-1}^{n}-\zeta_{i+1,j-1}^{n}-\zeta_{i-1,j+1}^{n})]+\gamma_3 f_{ij}^{n}(\zeta_{i,j+1}^{n}-\zeta_{i,j-1}^{n})\},\end{aligned} \tag{A 1}$$

where

$$A_{ij}^{n} = [1+2\gamma_1(1+a_{ij}^{n})]^{-1}, \tag{A 2}$$

$$\gamma_1 = \frac{k}{h^2\alpha^2}, \tag{A 3}$$

$$\gamma_2 = \frac{k}{h^2 St}, \tag{A 4}$$

$$\gamma_3 = \frac{k}{h}, \tag{A 5}$$

$$a_{ij}^{n} = (p_{1ij}^{n})^2+(p_{2ij}^{n})^2, \tag{A 6}$$

$$b_{ij}^{n} = \tfrac{1}{2}p_{1ij}^{n}, \tag{A 7}$$

$$c_{ij}^{n} = 2a_{ij}^{n}+hp_{3ij}^{n}, \tag{A 8}$$

$$d_{ij}^{n} = 2a_{ij}^{n}-hp_{3ij}^{n}, \tag{A 9}$$

$$e_{ij}^{n} = p_{2ij}^{n}, \tag{A 10}$$

$$f_{ij}^{n} = p_{4ij}^{n}. \tag{A 11}$$

The finite-difference expression to be satisfied by the stream function ψ is

$$\begin{aligned}-h^2\zeta_{ij} = -2(1+a_{ij})\,\psi_{ij}+\psi_{i+1,j}+\psi_{i-1,j}+\tfrac{1}{2}c_{ij}\,\psi_{i,j+1}+\tfrac{1}{2}d_{ij}\,\psi_{i,j-1} \\ +\tfrac{1}{2}e_{ij}(\psi_{i+1,j+1}+\psi_{i-1,j-1}-\psi_{i+1,j-1}-\psi_{i-1,j+1}),\end{aligned} \tag{A 12}$$

in which all quantities are evaluated at the current time level.

The expressions for vorticity at the walls and at the outlet boundary are given below. The suffix 0 denotes the boundary node in question, and lower-case letters as

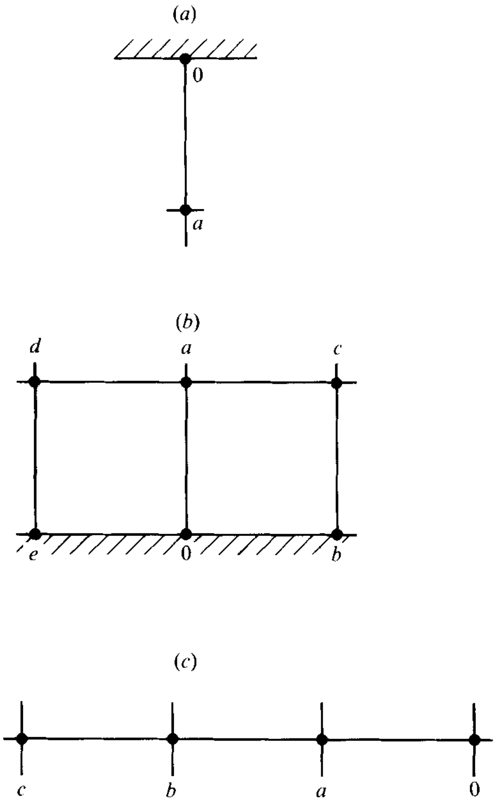

FIGURE 15. Nomenclature for nodes near the boundaries: (*a*) upper wall; (*b*) indentation region of lower wall; (*c*) outflow boundary.

suffices denote nodes nearby, as shown in figure 15. Thus at $z = 1$ (figure 15*a*), we have

$$h^2\zeta_0 = 3(p_{10})^2\,(\psi_0-\psi_a)-\tfrac{1}{2}h^2\zeta_a, \tag{A 13}$$

and at $z = 0$ (figure 15*b*),

$$h^2\zeta_0 = 3[(p_{10})^2+(p_{20})^2]\,(\psi_0-\psi_a)-\tfrac{1}{2}h^2\zeta_a-p_{20}(\psi_c+\psi_e-\psi_b-\psi_d)-\tfrac{3}{2}(\psi_b+\psi_e-2\psi_0). \tag{A 14}$$

Finally, at the outlet boundary (figure 15*c*), we have

$$\zeta_0 = 3\zeta_a-3\zeta_b+\zeta_c. \tag{A 15}$$

REFERENCES

ARMALY, B. F., DURST, F., PEREIRA, J. C. F. & SCHONUNG, B. 1983 Experimental and theoretical investigation of backward-facing step flow. *J. Fluid Mech.* **127**, 473–496.

BERTRAM, C. D. & PEDLEY, T. J. 1983 Steady and unsteady separation in an approximately two-dimensional indented channel. *J. Fluid Mech.* **130**, 315–345.

BORGAS, M. S. 1986 Waves, singularities and non-uniqueness in channel and pipe flows. Ph.D. dissertation, Cambridge University.

BRANDT, A. 1977 Multi-level adaptive solutions to boundary-value problems. *Maths Comp.* **31**, 333–390.

CANCELLI, C. & PEDLEY, T. J. 1985 A separated-flow model for collapsible-tube oscillations. *J. Fluid Mech.* **157**, 375–404.

CHERDRON, W., DURST, F. & WHITELAW, J. H. 1978 Asymmetric flows and instabilities in symmetric ducts with sudden expansions. *J. Fluid Mech.* **84**, 13–31.

DALY, B. J. 1974 A numerical study of pulsatile flow through constricted arteries. In *Proc. 4th Intl Conf. on Numerical Methods in Fluid Dynamics* (ed. R. D. Richtmeyer). Lecture Notes in Physics, vol. 35, pp. 117–124. Springer.

DRITSCHEL, D. G. 1988 Contour surgery: a topological reconnection scheme for extended integrations using contour dynamics. *J. Comput. Phys* (in the press).

DUCK, P. W. 1985 Laminar flows over unsteady humps: the formation of waves. *J. Fluid Mech.* **160**, 465–498.

HUNG, T.-K. & SCHUESSLER, G. B. 1977 An analysis of the hemodynamics of the opening of aortic valves. *J. Biomech.* **10**, 597–606.

KU, D. N., GIDDENS, D. P., ZARINS, C. K. & GLAGOV, S. 1985 Pulsatile flow and atherosclerosis in the human carotid bifurcation: positive correlation between plaque location and low and oscillatory shear stress. *Arteriosclerosis* **5**, 293–302.

MCKEE S. & MITCHELL, A. R. 1970 Alternating direction methods for parabolic equations in two space dimensions with a mixed derivative. *Comp. J.* **13**, 81–86.

PEDLEY, T. J. & STEPHANOFF, K. D. 1985 Flow along a channel with a time-dependent indentation in one wall: the generation of vorticity waves. *J. Fluid Mech.* **160**, 337–367.

PESKIN, C. S. 1972 Flow patterns around heart valves: a numerical method. *J. Comput. Phys.* **10**, 252–271.

PESKIN, C. S. 1977 Numerical analysis of blood flow in the heart. *J. Comput. Phys.* **25**, 220–252.

RALPH, M. E. 1986 Oscillatory flows in wavy-walled tubes. *J. Fluid Mech.* **168**, 515–540.

ROACHE, P. J. 1976 *Computational Fluid Dynamics*, 2nd Edn. Albuquerque: Hermosa.

ROBERTSON, J. M., CLARK, M. E. & CHENG, L. C. 1982 A study of the effects of a transversely moving boundary on plane Poiseuille flow. *J. Biomech. Engng* **104**, 314–323.

SCHUMANN, U. 1975 Linear stability of finite difference equations for three-dimensional flow problems. *J. Comput. Phys.* **18**, 465–470.

SMITH, F. T. 1986 Two-dimensional disturbance travel, growth and spreading in boundary layers. *J. Fluid Mech.* **169**, 353–377.

SMITH, F. T. & BODONYI, R. J. 1985 On short-scale inviscid instabilities in flow past surface-mounted obstacles and other non-parallel motions. *Aero. J.* June/July, 205–212.

SMITH, F. T. & BURGGRAF, O. R. 1985 On the development of large-sized, short-scaled disturbances in boundary layers. *Proc. R. Soc. Lond.* A **399**, 25–55.

SOBEY, I. J. 1980 On flow through furrowed channels. Part 1. Calculated flow patterns. *J. Fluid Mech.* **96**, 1–26.

SOBEY, I. J. 1985 Observation of waves during oscillatory channel flow. *J. Fluid Mech.* **151**, 395–426.

STEPHANOFF, K. D., PEDLEY, T. J., LAWRENCE, C. J. & SECOMB, T. W. 1983 Fluid flow along a channel with an asymmetric oscillating constriction. *Nature* **305**, 692–695.

STERN, M. E. & PRATT, L. J. 1985 Dynamics of vorticity fronts. *J. Fluid Mech.* **161**, 513–532.

TUTTY, O. R. & COWLEY, S. J. 1986 On the stability and the numerical solution of the unsteady interactive boundary-layer equation. *J. Fluid Mech.* **168**, 431–456.

VIECELLI, J. A. 1971 A computing method for incompressible flows bounded by moving walls. *J. Comput. Phys.* **8**, 119–143.